



Characterizing the Roughness in Channel Flows Using Direct Numerical Simulations

Akshay Patil¹ and Oliver Fringer²

Abstract: Turbulent flows over bumpy walls are ubiquitous and pose a fundamental challenge to various engineering applications such as coastal boundary layers, drag on ships, hydraulic conveyance networks, and bluff body aerodynamics, to name a few. In this study, we used direct numerical simulations (DNS) along with a direct-forcing immersed boundary method (IBM) to understand the connection between the roughness geometry and the mean flow drag. A bumpy wall was constructed using an array of randomly oriented ellipsoids characterized by the Corey shape factor (C_o). We found that our results exactly validated the experimental studies by Nikuradse for sand-grain type roughness ($C_o = 1.0$). Additionally, we observed that the mean flow drag increased for decreasing C_o through an increase in the form-drag contribution and a decrease in the viscous drag. We also developed a relationship between the statistics of the bottom height distribution and the roughness parameter (z_0) that may help explain the spread observed in the drag coefficient predicted when using conventional tools such as the Moody diagram. DOI: 10.1061/JHEND8.HYENG-13666. This work is made available under the terms of the Creative Commons Attribution 4.0 International license, <https://creativecommons.org/licenses/by/4.0/>.

Introduction

Turbulent boundary layers over rough walls are of significant interest to a variety of disciplines including the aviation industry (Spalart and Mclean 2011), shipping industry (Murphy et al. 2018), hydraulic conveyance networks (Moody 1944), and estuarine or coastal modeling (Grant and Madsen 1986), to name a few. A thorough review of recent advances in characterization of the flow drag over rough walls was presented by Chung et al. (2021). They showed a large uncertainty of roughly $\pm 11\%$ still exists in most engineering applications of flow drag prediction. Although the absolute magnitude of the uncertainty may not seem substantial, the same study suggested that these uncertainties have an expected cost of the order of billions of US dollars annually for naval applications (Chung et al. 2021). Consequently, understanding the uncertainty around the flow drag is a fruitful endeavor not only from a fundamental turbulence physics standpoint but from an engineering application perspective. Thus, a central question has aimed at specifying the flow drag as a function of the properties of the underlying roughness features.

Canonical flat-wall channel flows have been extensively studied because they encapsulate rich turbulence dynamics that support a wide range of applications (Kim et al. 1987; Tamburrino and Gulliver 1999; López and García 1999; Lozano-Durán et al. 2012; Rodi 2017). These studies have validated the analytical predictions of the time-averaged velocity profile close to the wall (i.e., the linear velocity region) and away from the wall (i.e., the log-law), as shown in Fig. 1. For canonical flat-wall channel flows, the

time-averaged velocity profile close to the wall obeys the law of the wall in that the velocity is linearly dependent on the distance from the wall (von Kármán 1930). This region is followed by the buffer layer that does not have a universal first principles-based model, even though most of the turbulence production occurs within this region (Pope 2000). Townsend (1976) suggested that in the region above the buffer layer, the time-averaged velocity profile is given by

$$\frac{\bar{U}}{u_*} = \frac{1}{\kappa} \ln \left(\frac{x_3 u_*}{\nu} \right) + B \quad (1)$$

where $u_* \equiv \sqrt{\tau/\rho_0}$ is the friction velocity; τ = bottom stress; ρ_0 = fluid density; κ = von Kármán constant; ν = kinematic viscosity of the fluid; and $B \approx 5.2$ = empirical constant, which is a weak function of the Reynolds number. This region is called the log-law region and has been the subject of a wide range of studies, as previously mentioned. As for the wake region above the log-law, there is some empirical understanding, although this region has received less attention than the others (Pope 2000).

Although flat-wall channels are relatively well understood, bumpy-wall channel flows have so far evaded such a universal understanding. The primary challenge has been to universally connect the roughness characteristics to the time-averaged velocity profile and bottom stress. Clauser (1954) and Hama (1954) independently proposed that roughness acts to shift the log-law region downward when compared to the flat-wall channel cases, as shown in Fig. 1. Consequently, the log-law velocity takes on the form

$$\frac{\bar{U}}{u_*} = \frac{1}{\kappa} \log \left(\frac{x_3 - \bar{k}_s}{z_0} \right) \quad (2)$$

where \bar{k}_s = mean physical roughness height; $z_0 \equiv \bar{k}_s/\alpha_k$ is the reference height that sets the location of the log-law; and α_k = regression parameter that best fits the log-law. Townsend (1976) hypothesized that for sufficient scale separation (i.e., large Reynolds number), the turbulence within the log-law region is self similar and that the wall boundary conditions set z_0 . Nikuradse (1933), in his seminal work, suggested that for sand-grain type roughness and large Reynolds numbers, the reference height for

¹Ph.D. Student, The Bob and Norma Street Environmental Fluid Mechanics Laboratory, Dept. of Civil and Environmental Engineering, Stanford Univ., Stanford, CA 94305 (corresponding author). ORCID: <https://orcid.org/0000-0001-9807-0733>. Email: alpatil@stanford.edu

²Professor, The Bob and Norma Street Environmental Fluid Mechanics Laboratory, Dept. of Civil and Environmental Engineering, Stanford Univ., Stanford, CA 94305. Email: fringer@stanford.edu

Note. This manuscript was submitted on February 2, 2023; approved on June 2, 2023; published online on September 15, 2023. Discussion period open until February 15, 2024; separate discussions must be submitted for individual papers. This paper is part of the *Journal of Hydraulic Engineering*, © ASCE, ISSN 0733-9429.

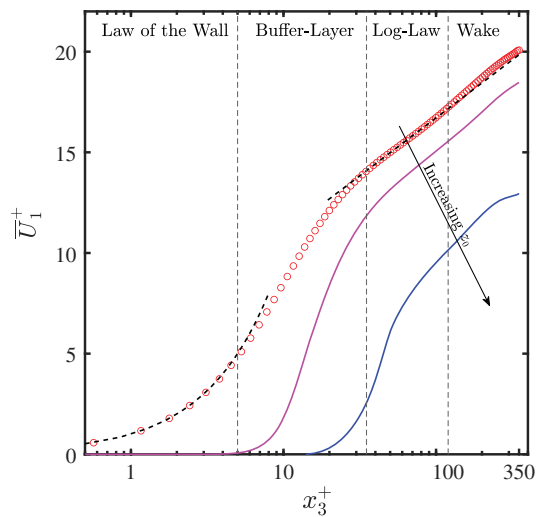


Fig. 1. (Color) Time-averaged velocity profiles for three cases with varying wall boundary conditions. The red markers correspond to canonical flat-wall channel flow, the magenta line corresponds to a bumpy-wall channel with hydraulically smooth wall conditions, and the blue line corresponds to a bumpy-wall channel with hydraulically transitional wall conditions. The text at the top of the figure marks the various regions in the canonical flat-wall channel case. These cases have identical friction Reynolds numbers (i.e., $Re_* \equiv u_* H / \nu = 350$).

bumpy walls is $z_0 = \bar{k}_s / 30$. Following the work by Nikuradse (1933), many studies have focused on characterizing non-sand grain type rough walls based on bulk statistics such as higher moments of the probability distribution of the roughness heights (Thakkar et al. 2017), regularly spaced identical roughness elements (Volino et al. 2011; Schultz and Flack 2009; Singh et al. 2007), and randomly oriented ellipsoidal roughness elements (Yuan and Piomelli 2014). Owing to the large number of nondimensional parameters needed to characterize the rough wall, most of the literature suggests a lack of universal scaling for the velocity shift in the transitionally rough flow regime. Thakkar et al. (2017) showed that the roughness characteristics such as the root-mean-squared roughness height can be used to characterize the peak turbulent kinetic energy for rough walls typically used in industrial

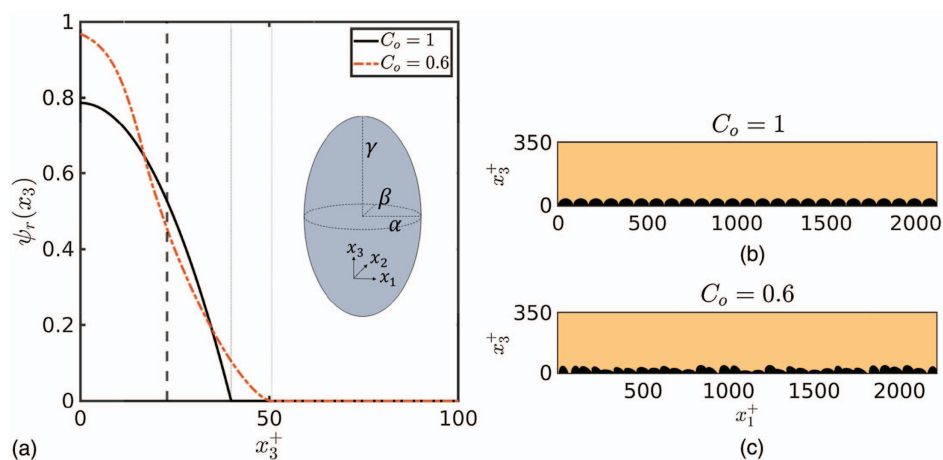


Fig. 2. (Color) (a) Comparison of the area fraction ψ_r as a function of distance from the wall (x_3^+) for identical mean roughness height (\bar{k}_s) and different Corey shape factor (C_o); inset provides a definition sketch for the ellipsoidal semiaxes α , β , and γ , respectively; and (b and c) the arrangement of individual roughness elements along the streamwise direction of the channel. The nondimensionalization is presented using the wall units corresponding to $Re_* = 350$.

applications. In geophysically relevant flows, Scotti (2006) validated a novel direct forcing immersed boundary method (IBM) with experimental results and observed that the turbulent statistics along with the dissipation characteristics can be accurately predicted. Scotti (2006) generated the bumpy wall using a set of randomly oriented ellipsoids, thus eliminating the dependence of streamwise and spanwise spacing length scales on the parameters of interest. This method has been further validated to understand the turbulent kinetic energy and Reynolds stress budgets in boundary layers (Yuan and Piomelli 2014, 2015).

The discussion presented in Scotti (2006) suggested that the bumpy wall generated using randomly oriented ellipsoids has a prescribed set of semiaxes lengths for the individual roughness elements. Using these lengths, we can define the Corey shape factor as (Corey 1949)

$$C_o = \frac{\alpha k_s}{\sqrt{(\beta k_s)(\gamma k_s)}} = \frac{\alpha}{\sqrt{\beta\gamma}} \quad (3)$$

where k_s = mean roughness height; α , β , and γ = nonzero constants defined such that αk_s = minor semiaxis length; βk_s = major semiaxis length; and γk_s = intermediate semiaxis length. Based on the shape characterization defined in Eq. (3), Scotti (2006) prescribed $C_o \approx 0.6$, which is expected to exhibit a mean flow drag that is larger than that for the case with roughness elements with $C_o = 1$, that is, sand-grain-type spherical roughness elements (Corey 1949; Julien 2010). The larger mean flow drag occurs due to flow separation because the roughness elements are relatively taller for $C_o = 0.6$ when compared to $C_o = 1.0$, thus increasing the form drag. Although the work of Corey (1949) dealt with the drag force on the vertical settling of sedimentary particles, the Corey shape factor can be used to characterize general properties of the roughness. For example, as shown in Fig. 2, for the same mean roughness height (\bar{k}_s), the roughness function can be different based on the Corey shape factor (C_o). These observations provide sufficient motivation to investigate the effect of changing C_o on the flow drag as a systematic characterization of engineering-based roughness features.

In this study, we quantified the effect of changing the Corey shape factor on the flow drag. Direct numerical simulations of a turbulent channel over varying C_o were used to present the first-order statistics and comment on the flow drag. Lower-cost

simulations with minimal-span channels were used to estimate the flow drag over a larger number of simulations with different C_o . Last, we connect the roughness characteristics to the expected mean flow drag and present concluding remarks.

Problem Formulation

Governing Equations and Computational Framework

We simulated a steady channel flow with direct numerical simulation (DNS) in which we solve the incompressible Navier–Stokes equations

$$\partial_i u_i + \partial_j (u_j u_i) = -\frac{1}{\rho_0} \partial_i p + \nu \partial_j \partial_j u_i + \Pi_c \delta_{i1} + F_{\text{IBM}} \quad (4)$$

subject to the continuity equation

$$\partial_i u_i = 0 \quad (5)$$

where t = time; u_i = velocity vector; x_j = coordinate vector; ρ_0 = density of the fluid; p = pressure; ν = kinematic viscosity of the fluid; Π_c = driving pressure gradient; δ_{ij} = Kronecker delta function; and F_{IBM} = immersed boundary force used to model the effect of the roughness elements. The coordinate axes x_1 , x_2 , and x_3 are aligned in the streamwise, spanwise, and vertical directions, respectively. The channel is periodic in the streamwise and spanwise directions, whereas a no-slip boundary condition is imposed at the bottom wall where the roughness elements are located. The top wall has boundary conditions given by

$$u_3(x_3 = H) = 0, \quad \frac{\partial u_i}{\partial x_3}(x_3 = H) = 0, \quad \forall i \in 1, 2 \quad (6)$$

where H = channel depth.

The governing equations were solved with a direct-numerical simulation code that had been extensively validated in previous studies of turbulent channel flows (Lozano-Durán and Bae 2016, 2019; Patil and Fringer 2022). In the code, all terms in the momentum equation are discretized in space with second-order accurate finite-difference schemes. In time, the fractional-step method (Kim and Moin 1985) is used along with a third-order accurate Runge–Kutta time-advancement scheme (Rai and Moin 1991). The advection terms are discretized in time explicitly, whereas the viscous terms are discretized implicitly to eliminate the stability constraint associated with viscous diffusion where the vertical grid resolution is refined. The pressure-Poisson equation was solved using a direct-Fourier-based method, as detailed in Costa (2018). Fourier transforms are applied in the x_1 (streamwise) and x_2 (spanwise) directions, which have uniform grid spacing, whereas a finite-difference method is applied in the vertical, which can have variable grid spacing. These discretizations result in tridiagonal systems for the horizontal Fourier modes that are solved efficiently with a tridiagonal solver. A bumpy wall was introduced with a direct forcing immersed boundary method based on the method proposed by Scotti (2006). The bumpy wall was generated by placing randomly oriented ellipsoids with fixed semiaxes such that the mean roughness height could be estimated a priori through the roughness function (ψ_r), which is the area fraction as a function of height, as shown in Fig. 2. Here, the area fraction at a given vertical coordinate is given by $A_f(x_3) = 2\pi^2 H^2 [1 - \psi_r(x_3)]$. Additional details of the computational framework can be found in Patil and Fringer (2022). As shown by Jiménez and Moin (1991) and Flores and Jiménez (2010), the near-wall, nonlinear turbulent kinetic energy production cycle maintains “healthy turbulence” for wall-bounded

flows. The study by Jiménez and Moin (1991) provided crucial insights into the statistical flow properties and elucidated the geometric requirements for “healthy turbulence” in channel flow geometries, also called minimal-span channels. This concept of the minimal-span channel was subsequently used to understand the mean flow drag without resolving the entire velocity profile (Chung et al. 2015; MacDonald et al. 2017). As the name indicates, the minimal-span channels limit the domain size in the spanwise direction such that the flow domain resolves the minimal dynamics (i.e., the interaction of two streamwise streaks) required to correctly resolve the near-wall region that is responsible for most of the turbulence production (Jiménez and Moin 1991; Flores and Jiménez 2010; Pope 2000). As a result, by correctly tuning the domain size in the spanwise direction, the mean velocity profile can be resolved adequately up to $x_3^+ \equiv x_3 u_* / \nu \approx 160$ (Jiménez and Moin 1991; Flores and Jiménez 2010; Chung et al. 2015; MacDonald et al. 2017).

Simulation Parameters

We define the drag coefficient as

$$C_d = \frac{u_*^2}{U^2} \quad (7)$$

where $u_* \equiv \sqrt{\tau/\rho_0}$ is the friction velocity; τ = time-averaged bottom stress averaged over the bottom boundary; and U = domain-integrated and time-averaged streamwise velocity. The friction velocity is fixed by choosing the driving pressure gradient $\Pi_c = u_*^2/H$, which in turn ensures that the bottom stress is given by $\tau = \rho_0 u_*^2$. As a result, because u_* is fixed, the drag coefficient changes due to changes in U . In this problem, there are seven relevant parameters: the bottom stress (τ/ρ_0), velocity (U), channel depth (H), kinematic viscosity of the fluid (ν), and the three semi-axis lengths of the ellipsoid ($\alpha \bar{k}_s$, $\beta \bar{k}_s$, and $\gamma \bar{k}_s$). Additionally, there are two rotation angles (uniformly distributed) that are required to define the Euler angle rotations of the ellipsoids. However, because there are a relatively large number of roughness elements, it is assumed that the effect of sampling the rotation angles is not substantial, as shown in Yuan and Piomelli (2014). Thus, using the Buckingham-pi theorem, the drag coefficient can be shown to have the functional dependence

$$C_d \equiv \frac{\tau}{\rho_0 U^2} \equiv \left(\frac{u_*}{U}\right)^2 = \mathcal{G}\left(\text{Re}, C_o, \frac{H}{\bar{k}_s}, S_p\right) \quad (8)$$

where $\text{Re} \equiv UH/\nu$ is the Reynolds number; C_o = Corey shape factor defined in Eq. (3); H/\bar{k}_s = blocking factor; and $S_p \equiv (\alpha\beta/\gamma^2)^{1/3}$ is the sphericity of the ellipsoids. In Eq. (8), the last three terms on the right-hand side of the equation depend on the statistical properties of the bed. Therefore, rather than conducting an exhaustive study of the effects of the bed parameters, we focused on the effects of C_o while holding H/\bar{k}_s fixed and then related the effective bottom roughness to the statistical properties of the bed. The sphericity (S_p) is not held constant, although we minimized its effects by ensuring $S_p \geq 0.84$.

To understand the effect of C_o , we chose friction Reynolds numbers 350 and 700, fixed $H/\bar{k}_s = 13.15$, and ran a set of full-span simulations along with a series of minimal-span channel flows to extend the range of C_o while limiting the computational cost. To directly compare the flat wall cases to the bumpy wall cases, Jiménez (2004) recommended $H/\bar{k}_s > 40$, such that the change in the effective depth does not significantly affect the comparison. However, because all the bumpy wall cases have identical values of H/\bar{k}_s , they can be compared directly. The relation $\langle \cdot \rangle^+ \equiv \langle \cdot \rangle u_* / \nu$ indicates

Table 1. Simulations carried out in this study, where the first $C(\text{num})$ corresponds to the friction Reynolds number, and the following $C(\text{num})$ stands for the Corey shape factor. Thus, case C350C1 corresponds to a channel with a friction Reynolds number of 350 and a Corey shape factor of 1. All simulations have $H/\bar{k}_s = 13.15$. Case names starting with the letter M correspond to the minimal-span channel simulations

Case name	Description	Re_*	C_o	S_p
CF	Flat wall, full-span channel	350	—	—
C350C1	Bumpy wall, full-span channel	350	1.0	1.000
C350C06	Bumpy wall, full-span channel	350	0.6	0.94
C700C1	Bumpy wall, full-span channel	700	1.0	1.000
C700C06	Bumpy wall, full-span channel	700	0.6	0.94
MC350C1	Bumpy wall, minimal-span channel	350	1.0	1.000
MC350C08	Bumpy wall, minimal-span channel	350	0.8	0.97
MC350C06	Bumpy wall, minimal-span channel	350	0.6	0.94
MC350C04	Bumpy wall, minimal-span channel	350	0.4	0.84
MC700C1	Bumpy wall, minimal-span channel	350	1.0	1.000
MC700C08	Bumpy wall, minimal-span channel	350	0.8	0.97
MC700C06	Bumpy wall, minimal-span channel	350	0.6	0.94
MC700C04	Bumpy wall, minimal-span channel	350	0.4	0.84

nondimensionalization using wall units unless specified otherwise. As shown in Table 1, we ran a set of 13 simulations to understand the effect of changing C_o and Re_* on the mean flow drag.

The full-span channels had dimensions $2\pi H \times \pi H \times H$ and were discretized using $768 \times 512 \times 256$ grid points in the streamwise, spanwise, and vertical directions, respectively. Uniform grid spacing was used to resolve the roughness region, beyond which hyperbolic tangent grid stretching was used. For $Re_* = 700$, this gave $\Delta x_1^+ = 5.73$, $\Delta x_2^+ = 4.30$, and $\Delta x_{3,\min}^+ = 0.66$ over the roughness region and $\Delta x_{3,\max}^+ = 10.0$ at the top of the channel. The dimensions of the minimal-span channels were $2\pi H \times 200\Delta x_2^+ \times H$ and discretized using $768 \times 64 \times 256$ grid points in the streamwise, spanwise, and vertical directions, respectively. For all simulations, a time-step size of $\Delta t^+ \equiv u_*^2 \Delta t / \nu = 0.045$ was used, based on a maximum Courant number of 0.4. All bumpy wall simulations corresponded to hydraulically transitional flow conditions, that is, $4 \leq u_* \bar{k}_s / \nu \leq 70$, with $u_* \bar{k}_s / \nu = 26.6$ and $u_* \bar{k}_s / \nu = 53.2$ for $Re_* = 350$ and $Re_* = 700$, respectively. Ideally, for DNS, higher-order methods are preferred, although the deficiencies inherent to the second-order accurate method can be alleviated with grid refinement for the requisite scales of interest, as discussed in Moin and Verzicco (2016). For the simulations carried out in this paper, the region that encapsulates the roughness features was uniformly discretized with a vertical grid resolution of $\Delta x_3^+ = 0.6 < 1.0$. This grid resolution accurately resolved the flow features that correctly predict the Reynolds-stress dynamics such that the relative residual in computing the turbulent kinetic energy budget was less than 5%. Additionally, implementing boundary conditions and the immersed boundary method are relatively straightforward for second-order numerical stencils when compared to higher-order stencils or spectral methods. As a result, despite the second-order accurate spatial discretization, the present computational framework ensured accurate simulation of turbulent flows without introducing additional computational costs while reducing the model complexity.

The channel flow simulations were initialized with a flow field from precursor simulations interpolated and scaled to match the friction Reynolds number. The simulations were run for a total of 15 eddy-turnover times ($T_\epsilon = H/u_*$) with an initial transient of $10T_\epsilon$. Time-averaged statistics discussed in this paper were averaged over the last $5T_\epsilon$ unless otherwise specified. The flow is said to be statistically converged when the total stress profile above the roughness elements follows the linear stress profile as discussed in Patil and Fringer (2022). The full-span channels were run on 256 central processing units (CPU) and required about 276,500 CPU hours to simulate a total of 15 eddy-turnover times for both values

of the Reynolds numbers. The minimal-span channels were run on 32 CPUs and required 7,700 CPU hours to simulate a total of 15 eddy-turnover times, reflecting savings in computational cost by a factor of 36 when compared to the full-span simulations.

Results

Mean and Root-Mean-Squared Velocity Profiles

Changing the parameters and their impact on the mean flow drag can be inferred by observing the location of the log-law region in the time-averaged and planform-averaged velocity profiles. Fig. 3(a) shows a comparison of the time-averaged and planform-averaged streamwise velocity for the full-span channel flow cases. Comparing the velocity profiles to the canonical flat-wall channel case (CF), the presence of roughness decreased the mean flow U and thus increased the bottom drag coefficient for the bumpy wall cases. The bumpy wall log-law is given by Eq. (2), where Nikuradse (1933) found that $z_0 = \bar{k}_s/30$ for sand-grain type roughness (i.e., $C_o = 1.0$). As shown in Fig. 3, the red dashed line corresponds to the log-law estimate given by Eq. (2) and the Nikuradse (1933) estimate for z_0 . Case C350C1 exactly matched this prediction, and, more importantly, z_0 was not regressed, unlike in the other cases (i.e., $C_o = 0.6$). The mean flow drag for case C700C1 was larger when compared to case C350C1 because the drag increased with increasing Re_* . A similar observation can be made when case C700C06 is compared to case C350C06. The full-span channel results suggest that there was a consistent increase in the mean flow drag when decreasing C_o for the two Re_* considered in this study.

To further understand the effect of C_o on the mean flow drag, we validated the use of minimal-span channels (Jiménez and Moin 1991; Chung et al. 2015; MacDonald et al. 2017). As seen in Fig. 3(a), as the spanwise domain was restricted to incorporate the interaction of just two streamwise streaks, the velocity profiles in the minimal-span channels matched the full-span counterparts for $x_3^+ \lesssim 160$, beyond which the profiles deviated from the log law. Therefore, because minimal-span channels accurately captured the near-wall velocity profiles, we used the minimal-span channels to extend the range of C_o without imposing the large computational cost that would be required for the full-span channel cases.

In addition to the mean velocity profiles, there were distinct changes observed in the root-mean-squared (RMS) velocity profiles, as shown in Fig. 3(b). First, for cases with $C_o = 0.6$, there was a

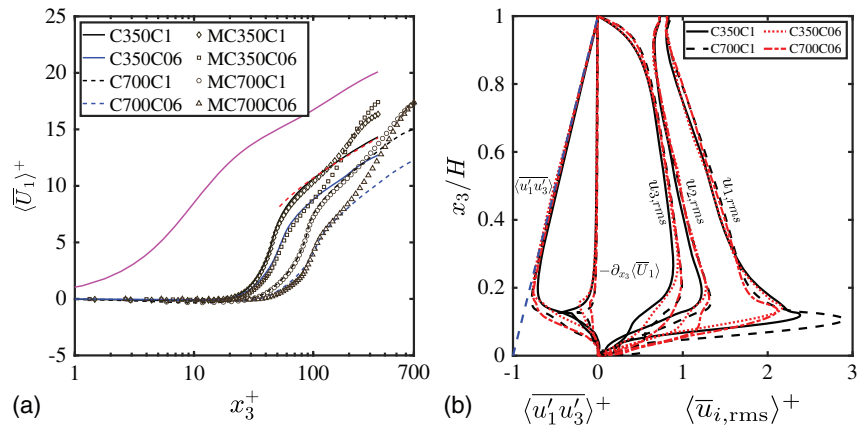


Fig. 3. (Color) (a) Comparison of time-averaged and planform-averaged velocity profiles for the full-span channel flow cases (lines) and minimal-span channel flow cases (markers). The magenta solid line marks the canonical channel flow case with $Re_* = 350$. The red dashed line marks the location of the log-law fit where $z_0 = \bar{k}_s/30$, as suggested by Nikuradse (1933). For clarity, the time-averaged and planform-averaged velocity profiles for cases MC350C08, MC350C04, MC700C08, and MC700C04 are not shown; and (b) comparison of the root-mean-squared (RMS) velocity profiles for the full-span channels (right of the zero mark on the x -axis) and the Reynolds and viscous stresses (left of the zero mark on the x -axis). The blue dashed line marks the total linear stress profile expected for channel flow cases.

strong decrease in the RMS velocity components when compared to the case with $C_o = 1.0$ in the near-wall region. Further away from the wall, cases with $C_o = 0.6$ were identical to those with $C_o = 1.0$, further confirming the decoupled nature of the near-wall and outer regions of the flow (Townsend 1976). Similar mean flow response for the two Reynolds numbers suggested that the effect of C_o was to modify the wall boundary condition such that decreasing values of C_o resulted in a larger effective z_0 . As for the Reynolds and viscous stress profiles, most of the variations occurred in the vicinity of the roughness elements. For the viscous stress, there was a prominent decrease in the maximum value with decreasing C_o . Additionally, as the friction Reynolds number increased, the relative contribution of the viscous stress decreased. These changes in the viscous stress profiles support the hypothesis that the stress contribution due to flow separation is expected to increase at the expense of the viscous stress for decreasing C_o (discussed later). The Reynolds stress profiles, on the other hand, were independent of C_o and followed the linear stress (blue dashed line) profile as expected.

Drag Coefficient

To compare the drag coefficient for the full-span and minimal-span channels, we define the drag coefficient

$$C_d^r = \left(\frac{u_*}{U_r} \right)^2 \quad (9)$$

where U_r = time-averaged and planform-averaged streamwise velocity evaluated at $x_3^+ = 120$. This definition of the drag coefficient allows for comparison of the full-span and minimal-span channels for cases where the full log-law velocity profile may not be available. Such a definition of the drag coefficient is quite common, especially in field experiments where only point measurements may be available (Egan et al. 2019). Fig. 4 shows a comparison of the drag coefficient for all cases detailed in Table 1. The overall trend was that with decreasing values of C_o , there was an increase in the drag coefficient for the two friction Reynolds numbers considered. Additionally, the drag coefficient predicted using the minimal-span channels was consistent with the full-span

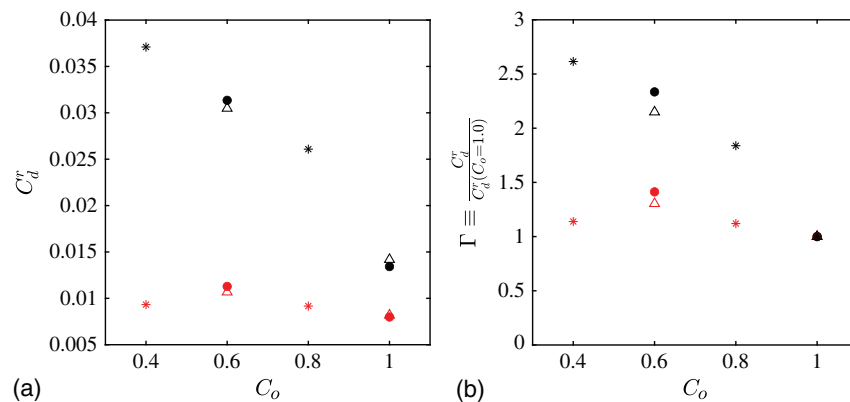


Fig. 4. (Color) (a) Comparison of the drag coefficient for varying values of the Corey shape factor (C_o). Filled data markers correspond to full-span channel cases, whereas empty markers correspond to minimal-span channel cases. Black markers indicate $Re_* = 700$, whereas red markers indicate $Re_* = 350$; and (b) same data as panel (a) but normalized using the drag coefficient for $C_o = 1$ such that the y -axis represents the relative gain (Γ) of the drag coefficient for decreasing C_o .

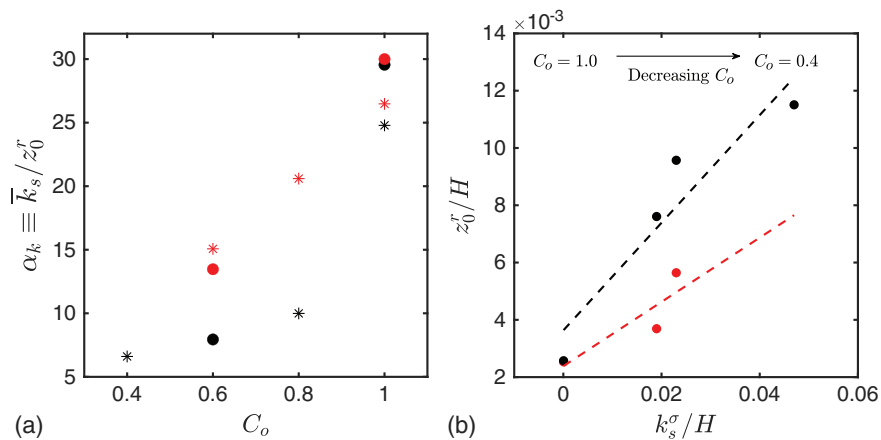


Fig. 5. (Color) (a) Comparison of the effect of changing C_o and Re_* on the roughness parameter z_0^r ; and (b) correlation between the standard deviation of the roughness (k_s^σ) and the roughness parameter (z_0^r). Dashed lines mark the linear fit to the data, and the markers starting from the left correspond to $C_o = 1.0$, $C_o = 0.8$, $C_o = 0.6$, and $C_o = 0.4$, respectively. Marker color scheme is identical to Fig. 4.

channels, providing further impetus to use the concept of minimal-span channels to predict the mean flow drag (Chung et al. 2015; MacDonald et al. 2017). For $Re_* = 350$, the drag coefficient increased as C_o decreased until about $C_o = 0.6$, beyond which C_d^r saturated and started to decrease slightly. However, for $Re_* = 700$, a monotonic increase in the drag coefficient was observed with decreasing C_o . Because the estimate of C_d^r is sensitive to z_{ref} , C_d^r seemed to saturate for $Re_* = 350$ but increased monotonically for $Re_* = 700$. Although it is unclear why case MC350C04 appears to be an outlier in the overall trend, it is omitted in the following analysis. The value of C_d^r was more sensitive to C_o for higher Re_* , which is a result of the higher contribution of the form drag at higher Re_* , as discussed later. It is expected that for increasing values of Re_* , the drag coefficient becomes independent of Re_* , similar to the behavior of pipe friction in the Moody chart. The independent behavior of the transition to Re_* is expected to occur at lower Re_* for increasing relative roughness such that once the flow is sufficiently hydraulically rough (i.e., $Re_k \gg 70$), the drag coefficient will asymptote to a constant value. Because of the relatively low values of Re_* in this paper, due to computational constraints, there was a nontrivial dependence of the mean flow drag on Re_* for identical values of the Corey shape factor. As a result, for identical values of C_o and \bar{k}_s , the mean flow drag changed nontrivially.

Another way to understand the effect of changing the geometry of the bumps is through changes in the roughness parameter z_0 , as shown in Fig. 5. For the full-span cases, z_0 can be regressed to best fit the log law [Eq. (2)] because the log-law region is well resolved. This is evident in Fig. 3, which shows that the minimal-span channels reproduced the full-span velocity profiles. However, for cases without companion full-span channels ($C_o = 0.4, 0.8$), the lack of a significant log law region did not allow such a regression to compute z_0 . Consequently, to enable consistent comparison between the full-span and minimal-span channels, z_0^r was inferred from the log law at a reference height of $z_{ref} = 120\nu/u_{*}$, such that

$$z_0^r = (z_{ref} - \bar{k}_s) \exp\left(-\frac{\kappa}{\sqrt{C_d^r}}\right) \quad (10)$$

where C_d^r = drag coefficient defined in Eq. (9). Fig. 5(a) suggests a similar overall trend as observed from the drag coefficient for changing C_o and Re_* . Additionally, it is clear that for increasing

values of C_o , α_k increased, suggesting that the roughness height z_0^r decreased for increasing C_o .

Although these observations provide a consistent way to relate the roughness characteristics, it is often more practical to relate the roughness height z_0^r to statistical properties of the bed height in addition to the mean roughness (bed) height. Indeed, the results in the paper show very clearly that the bottom drag varied significantly through changes in C_o even though \bar{k}_s was constant for all simulations. To relate z_0 to the statistical properties of the bed, we calculated the standard deviation of the bed height

$$k_s^\sigma = \left[\frac{1}{N} \sum_{i=1}^N (k_s^i - \bar{k}_s)^2\right]^{1/2} \quad (11)$$

where k_s^i = height of each of the ellipsoids; and $N \approx 360$ is the number of ellipsoids (N is approximate because the number of ellipsoids that can fit on the bottom wall is subject to the random orientation angles). We then regressed the standard deviation to the roughness height with $z_0^r = \chi k_s^\sigma$, where χ is the regression parameter. As shown in Fig. 5(b), good correlation can be observed between k_s^σ and the roughness parameter; that is, z_0^r , where $\chi(Re_* = 700) = 0.188$ and $\chi(Re_* = 350) = 0.112$. For $Re_* = 350$, the data point for $C_o = 0.4$ was not included in the regression because it appears to be an outlier. Although it is unclear why this point was an outlier, we expect this to be a consequence of the minimal-span nature of the channel. Using linear regression, we observed $R^2 = 0.891$ for $Re_* = 700$, and $R^2 = 0.765$ for $Re_* = 350$, suggesting a strong correlation between the roughness characteristics and the expected roughness parameter. In addition to the Re_* dependence, the definition of C_o does not account for varying values of the sphericity (S_p) for identical C_o , as suggested by Julien (2010). It is clear to see that z_0^r is sensitive to Re_* , which can be inferred from the regression parameter. Some of the scatter observed in the data presented here can be attributed to the transitional roughness Reynolds number regime because the flow separation was localized to some roughness elements that penetrated beyond the viscous sublayer, as shown in Fig. 6 and discussed in Schultz and Myers (2003) and Flack et al. (2012). These observations may help explain the variability observed in conventional methods to estimate the mean flow drag (e.g., Moody 1944) or the roughness function (ΔU^+) defined in Schultz and Myers (2003).

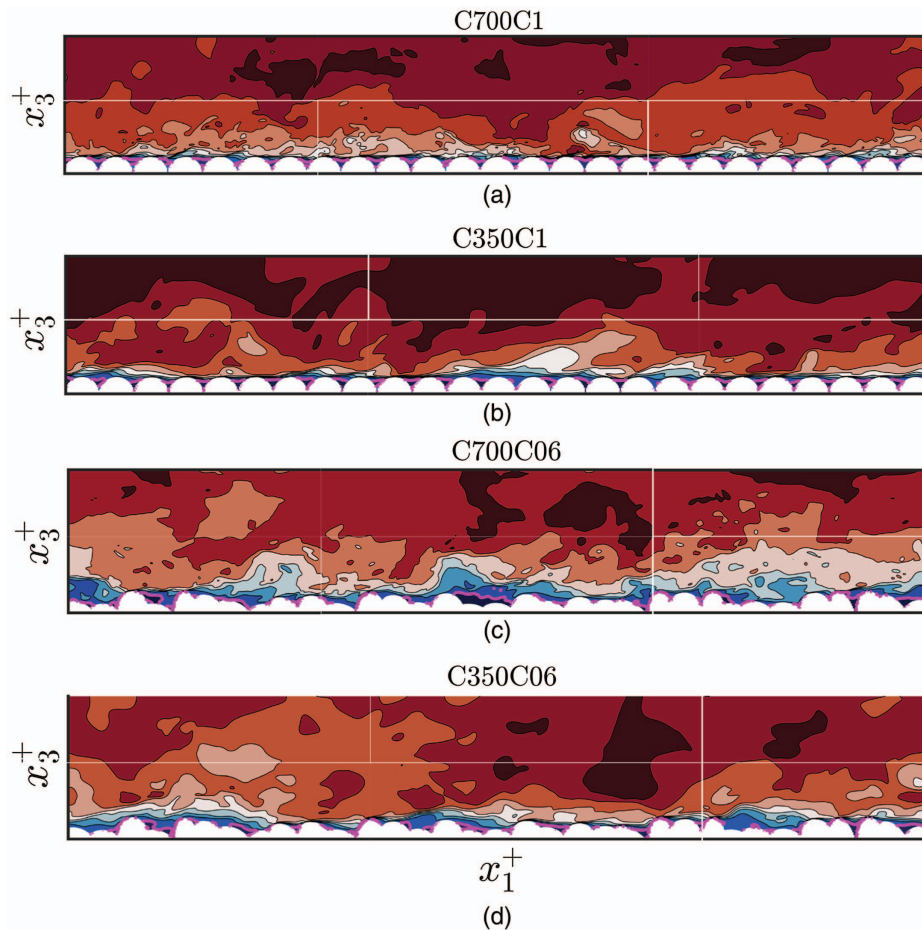


Fig. 6. (Color) Contour plots along the channel centerline at time $t_c = tu_*/H = 12.0$, showing the instantaneous streamwise velocity normalized by the friction velocity (u_1/u_*) for the four full-span channel cases. The white region marks the roughness elements. Blue color indicates slower velocities, and red color indicates faster velocities. The solid magenta line marks the contour where $U_1 = 0$; thus, regions enclosed by the magenta line correspond to negative streamwise velocity where there is flow separation. (a) C700C1; (b) C350C06; (c) C700C06; and (d) C350C06.

Mean Momentum Partitioning

Increased mean flow drag with a simultaneous decrease in the viscous stress for decreased C_o suggests that there was a net increase in the form drag components as the flow separated at the crest of the roughness elements. As shown in Fig. 6, there was relatively more flow separation for cases C350C06 and C700C06 when compared to cases C350C1 and C700C1. These observations, along with the attenuated viscous stress profiles and increased drag coefficient, suggest that the form drag for smaller C_o increased. In addition to Fig. 6, a vorticity comparison can be seen in Fig. 7, which shows instantaneous vorticity for the four full-span cases. Comparing cases with $Re_* = 350$ against $Re_* = 700$ clearly shows the effect of increased Reynolds number on the vorticity distribution close to the wall. The effect of C_o was more pronounced for lower Re_* , as indicated by the slightly more negative values for case C350C06 when compared to case C350C1. For higher Re_* , there were no obvious differences in the vorticity between cases C700C1 and C700C06.

Because the immersed boundary force (F_{IBM}) is imposed at every substep in the Runge–Kutta time-integration scheme, only the divergence-free velocity at the end of each time step is available (Yuan and Piomelli 2014, 2015). Therefore, although the IBM force can be used to compare the total drag force on the bed, it does not give the relative contributions of viscous and form drag.

To separately compute these components of the drag, we began with the streamwise momentum equation

$$\partial_t u_1 + \partial_j (u_j u_1) = -\partial_1 P + \nu \partial_j \partial_j u_1 + \Pi_c + F_{IBM} \quad (12)$$

where $P = p/\rho_0 =$ modified or reduced pressure. Defining \mathcal{V}_f as the volume occupied by the fluid above the roughness elements and integrating Eq. (12) over \mathcal{V}_f gives, after using Gauss's theorem and noting that $F_{IBM} = 0$ in \mathcal{V}_f and imposing periodicity in the x_1 and x_2 directions and free-slip condition at $x_3 = H$,

$$\begin{aligned} \partial_t \int_{\mathcal{V}_f} u_1 d\mathcal{V} + \int_{\mathcal{A}_B} u_1 (u_j e_j) d\mathcal{A} \\ = - \int_{\mathcal{A}_B} P e_1 d\mathcal{A} + \nu \int_{\mathcal{A}_B} e_j \partial_j u_1 d\mathcal{A} + \mathcal{V}_f \Pi_c \end{aligned} \quad (13)$$

where $\mathcal{A}_B =$ control surface at the bumpy wall that corresponds to the top of the roughness elements; and $e_j =$ unit normal vector pointing outward relative to \mathcal{V}_f . After time-averaging Eq. (13), the unsteady term vanishes, thus giving the momentum partitioning

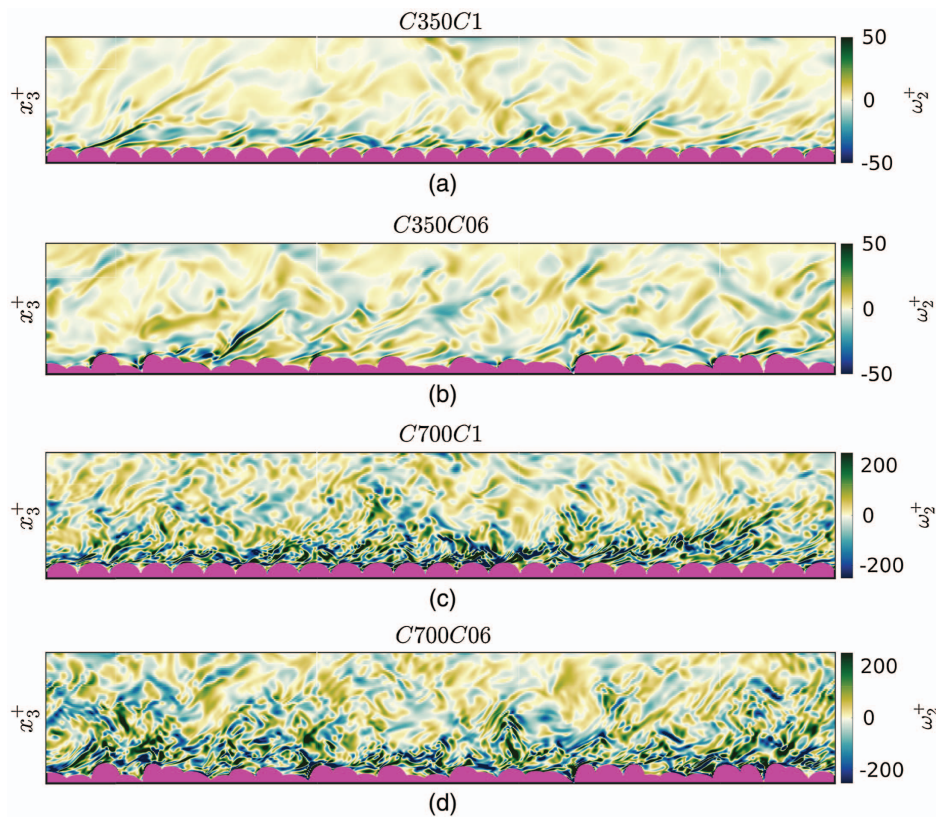


Fig. 7. (Color) Contour plots along the channel centerline of the spanwise vorticity $\omega_2^+ = \omega_2 \nu / u_*^2$ at time $t_c = tu_* / H = 14.0$. The magenta region marks the roughness elements. (a) C350C1; (b) C350C06; (c) C700C1; and (d) C700C06.

$$\underbrace{\int_{A_B} \overline{u_1 u_j} e_j dA}_{\text{Advective Term}} + \underbrace{\int_{A_B} \overline{P} e_1 dA}_{\text{Form Drag}} - \underbrace{\nu \int_{A_B} e_j \partial_j \overline{u_1} dA}_{\text{Viscous Drag}} = \underbrace{\mathcal{V}_f \Pi_c}_{\text{Driving Force}} \quad (14)$$

where the overbar represents the time average. The advective term on the left-hand side is nonzero because the IBM method imposes a force that produces a vanishing cell-centered velocity component and a small nonzero face-centered component where A_B is defined. As a result, the advective term does not vanish, although it is much smaller than the other terms. Table 2 lists

Table 2. Mean momentum partition computed using the discrete integration of the streamwise momentum equation. All terms are normalized by u_*^2 / H

Case name	Form drag	Viscous drag	Advective term	Sum
C700C1	0.773	0.214	0.017	1.00
C350C1	0.734	0.242	0.028	1.00
C700C06	0.863	0.129	0.011	1.00
C350C06	0.823	0.172	0.014	1.00
MC700C1	0.785	0.193	0.022	1.00
MC350C1	0.742	0.228	0.030	1.00
MC700C08	0.810	0.171	0.019	1.00
MC350C08	0.767	0.209	0.023	1.00
MC700C06	0.869	0.116	0.015	1.00
MC350C06	0.820	0.160	0.020	1.00
MC700C04	0.872	0.111	0.017	1.00

the normalized contribution of the three terms in the mean momentum equations for the full-span channel flow cases. The results indicate an enhanced form drag component for $C_o = 0.6$ that can be interpreted as a consequence of increased flow separation because the roughness elements are taller when compared to the case with $C_o = 1.0$. Additionally, this increase in the form drag occurs with a simultaneous decrease in the viscous drag for the two Reynolds numbers. Because the driving pressure gradient (i.e., u_*^2 / H) is constant for varying C_o for a given Re_* , only the bottom boundary conditions are responsible for an increase in the drag coefficient and the mean momentum partition. It is clear from Table 2 that there was a definitive increase in the form drag for decreasing C_o for both Re_* .

The relative importance of the viscous and form drag (relative drag) is depicted for varying C_o in Fig. 8. The minimal span channels capture the overall trend as predicted by the full span channels, with a consistent overprediction for all cases when compared to the full span data. As shown in Fig. 3, the time-averaged and planform-averaged velocity profiles for the minimal-span channels led to a flow velocity that was comparatively large in magnitude away from the wall. Because the minimal-span channels did not effectively mix momentum in the vertical direction due to the spanwise domain constraint, we anticipated larger form drag as a result of this increased mean flow velocity away from the wall when compared to the full-span channel cases (Chung et al. 2015; Yuan and Piomelli 2015). For both values of Re_* , the relative drag increased for decreasing values of C_o . Additionally, it is clear from these data that the relative drag increased more quickly for $Re_* = 700$ when compared to $Re_* = 350$, further validating the changes observed in C_d^r (see Fig. 4).

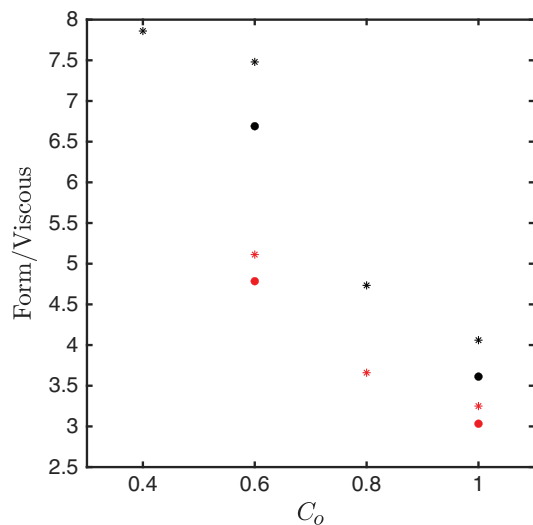


Fig. 8. (Color) Comparison of the ratio of the form drag to the viscous drag for varying C_o . Black markers correspond to $Re_* = 700$, and red markers correspond to $Re_* = 350$. Full-span channels are denoted by filled circles, and minimal-span channels are denoted using asterisk markers.

Conclusions

We studied the effect of changing bottom boundary conditions through the definition of the Corey shape factor that characterizes the individual roughness elements on the mean flow drag. Using a combination of full-span and minimal-span channel flows and direct numerical simulations, we established that decreasing Corey shape factors result in increased mean flow drag. Additionally, we validated that for sand-grain-type roughness with $C_o = 1.0$, DNS can accurately replicate the Nikuradse (1933) estimate $z_0 \equiv \bar{k}_s/30$ without regression. We also observed that for decreasing values of C_o , there was enhanced flow separation for the two friction Reynolds numbers considered in this study. Furthermore, using a mean momentum analysis, we demonstrated that this increased mean flow drag was a result of enhanced flow separation at the crest of the roughness elements that led to a larger form drag contribution. Additionally, we showed that the viscous drag decreased with the simultaneous increase in the form drag where these changes are both a function of the flow Reynolds number and the Corey shape factor. This study also explains variations in the drag coefficient (C_d or C_f), which is typically assumed to be only a function of the mean roughness height (\bar{k}_s). The drag coefficient was observed to be 2.5 times larger for $C_o = 0.4$ when compared to the drag coefficient when $C_o = 1.0$ for identical mean roughness height (\bar{k}_s) for $Re_* = 700$. Additionally, the roughness parameter correlated well with the standard deviation of the roughness height for varying C_o , thus providing a means to estimate the mean flow drag using the roughness characteristics.

Data Availability Statement

All the data or codes that support the findings of this study are available from the corresponding author upon reasonable request.

Acknowledgments

This research was supported by NSF Award OCE 1736668. We would like to thank Stanford University and the Stanford Doerr

School for Sustainability (SDSS) Center for Computation for providing computational resources and support that contributed to these research results. We also thank Adrian Lozano-Duran for providing the computational core of the finite-difference code used in this study.

References

- Chung, D., L. Chan, M. MacDonald, N. Hutchins, and A. Ooi. 2015. "A fast direct numerical simulation method for characterising hydraulic roughness." *J. Fluid Mech.* 773 (Jun): 418–431. <https://doi.org/10.1017/jfm.2015.230>.
- Chung, D., N. Hutchins, M. P. Schultz, and K. A. Flack. 2021. "Predicting the drag of rough surfaces." *Annu. Rev. Fluid Mech.* 53 (Jan): 439–471. <https://doi.org/10.1146/annurev-fluid-062520-115127>.
- Clauser, F. H. 1954. "Turbulent boundary layers in adverse pressure gradients." *J. Aeronaut. Sci.* 21 (2): 91–108. <https://doi.org/10.2514/8.2938>.
- Corey, A. T. 1949. "Influence of shape on the fall velocity of sand grains." M.S. thesis, Agricultural and Mechanical College, Colorado State Univ.
- Costa, P. 2018. "A FFT-based finite-difference solver for massively-parallel direct numerical simulations of turbulent flows." *Comput. Math. Appl.* 76 (8): 1853–1862. <https://doi.org/10.1016/j.camwa.2018.07.034>.
- Egan, G., M. Cowherd, O. Fringer, and S. Monismith. 2019. "Observations of near-bed shear stress in a shallow, wave- and current-driven flow." *J. Geophys. Res. Oceans* 124 (8): 6323–6344. <https://doi.org/10.1029/2019JC015165>.
- Flack, K. A., M. P. Schultz, and W. B. Rose. 2012. "The onset of roughness effects in the transitionally rough regime." *Int. J. Heat Fluid Flow* 35 (Jun): 160–167. <https://doi.org/10.1016/j.ijheatfluidflow.2012.02.003>.
- Flores, O., and J. Jiménez. 2010. "Hierarchy of minimal flow units in the logarithmic layer." *Phys. Fluids* 22 (7): 071704. <https://doi.org/10.1063/1.3464157>.
- Grant, W. D., and O. S. Madsen. 1986. "The continental-shelf bottom boundary layer." *Annu. Rev. Fluid Mech.* 18 (1): 265–305. <https://doi.org/10.1146/annurev.fl.18.010186.001405>.
- Hama, F. R. 1954. "Boundary layer characteristics for smooth and rough surfaces." *Trans. Soc. Nav. Architects Mar. Eng.* 62 (Mar): 333–358.
- Jiménez, J. 2004. "Turbulent flows over rough walls." *Annu. Rev. Fluid Mech.* 36 (1): 173–196. <https://doi.org/10.1146/annurev.fluid.36.050802.122103>.
- Jiménez, J., and P. Moin. 1991. "The minimal flow unit in near-wall turbulence." *J. Fluid Mech.* 225 (Apr): 213–240. <https://doi.org/10.1017/S0022112091002033>.
- Julien, P. Y. 2010. *Erosion and sedimentation*. 2nd ed. Cambridge, UK: Cambridge University Press.
- Kim, J., and P. Moin. 1985. "Application of a fractional-step method to incompressible Navier–Stokes equations." *J. Comput. Phys.* 59 (2): 308–323. [https://doi.org/10.1016/0021-9991\(85\)90148-2](https://doi.org/10.1016/0021-9991(85)90148-2).
- Kim, J., P. Moin, and R. Moser. 1987. "Turbulence statistics in fully developed channel flow at low Reynolds number." *J. Fluid Mech.* 177 (Apr): 133–166. <https://doi.org/10.1017/S0022112087000892>.
- López, F., and M. H. García. 1999. "Wall similarity in turbulent open-channel flow." *J. Eng. Mech.* 125 (7): 789–796. [https://doi.org/10.1061/\(ASCE\)0733-9399\(1999\)125:7\(789\)](https://doi.org/10.1061/(ASCE)0733-9399(1999)125:7(789)).
- Lozano-Durán, A., and H. J. Bae. 2016. "Turbulent channel with slip boundaries as a benchmark for subgrid-scale models in LES." *Annu. Res. Briefs* 2016 (Jan): 97–103.
- Lozano-Durán, A., and H. J. Bae. 2019. "Characteristic scales of Townsend's wall-attached eddies." *J. Fluid Mech.* 868 (Jun): 698–725. <https://doi.org/10.1017/jfm.2019.209>.
- Lozano-Durán, A., O. Flores, and J. Jiménez. 2012. "The three-dimensional structure of momentum transfer in turbulent channels." *J. Fluid Mech.* 694 (Mar): 100–130. <https://doi.org/10.1017/jfm.2011.524>.
- MacDonald, M., D. Chung, N. Hutchins, L. Chan, A. Ooi, and R. Garca-Mayoral. 2017. "The minimal-span channel for rough-wall turbulent flows." *J. Fluid Mech.* 816 (Apr): 5–42. <https://doi.org/10.1017/jfm.2017.69>.

- Moin, P., and R. Verzicco. 2016. "On the suitability of second-order accurate discretizations for turbulent flow simulations." *Eur. J. Mech. B. Fluids* 55 (Jan): 242–245. <https://doi.org/10.1016/j.euromechflu.2015.10.006>.
- Moody, F. 1944. "Friction factors for pipe flow." *Trans. ASME* 66 (Nov): 671–684.
- Murphy, E. A. K., J. M. Barros, M. P. Schultz, K. A. Flack, C. N. Steppe, and M. A. Reidenbach. 2018. "Roughness effects of diatomaceous slime fouling on turbulent boundary layer hydrodynamics." *Biofouling* 34 (9): 976–988. <https://doi.org/10.1080/08927014.2018.1517867>.
- Nikuradse, J. 1933. "Strömungsgesetze in rauhen Röhren." In *VDI-Forschungsheft*, 361. Berlin, Germany: VDI-Verlag.
- Patil, A., and O. Fringer. 2022. "Drag enhancement by the addition of weak waves to a wave-current boundary layer over bumpy walls." *J. Fluid Mech.* 947 (Sep): A3. <https://doi.org/10.1017/jfm.2022.628>.
- Pope, S. B. 2000. *Turbulent flows*. Cambridge, UK: Cambridge University Press.
- Rai, M. M., and P. Moin. 1991. "Direct simulations of turbulent flow using finite-difference schemes." *J. Comput. Phys.* 96 (1): 15–53. [https://doi.org/10.1016/0021-9991\(91\)90264-L](https://doi.org/10.1016/0021-9991(91)90264-L).
- Rodi, W. 2017. "Turbulence modeling and simulation in hydraulics: A historical review." *J. Hydraul. Eng.* 143 (5): 03117001. [https://doi.org/10.1061/\(ASCE\)HY.1943-7900.0001288](https://doi.org/10.1061/(ASCE)HY.1943-7900.0001288).
- Schultz, M. P., and K. A. Flack. 2009. "Turbulent boundary layers on a systematically varied rough wall." *Phys. Fluids* 21 (Jan): 015104. <https://doi.org/10.1063/1.3059630>.
- Schultz, M. P., and A. Myers. 2003. "Comparison of three roughness function determination methods." *Exp. Fluids* 35 (Oct): 372–379. <https://doi.org/10.1007/s00348-003-0686-x>.
- Scotti, A. 2006. "Direct numerical simulation of turbulent channel flows with boundary roughened with virtual sandpaper." *Phys. Fluids* 18 (3): 031701. <https://doi.org/10.1063/1.2183806>.
- Singh, K. M., N. D. Sandham, and J. J. R. Williams. 2007. "Numerical simulation of flow over a rough bed." *J. Hydraul. Eng.* 133 (4): 386–398. [https://doi.org/10.1061/\(ASCE\)0733-9429\(2007\)133:4\(386\)](https://doi.org/10.1061/(ASCE)0733-9429(2007)133:4(386)).
- Spalart, P. R., and J. D. Mclean. 2011. "Drag reduction: Enticing turbulence, and then an industry." *Phil. Trans. R. Soc. A* 369 (Apr): 1556–1569.
- Tamburrino, A., and J. S. Gulliver. 1999. "Large flow structures in a turbulent open channel flow." *J. Hydraul. Res.* 37 (3): 363–380. <https://doi.org/10.1080/00221686.1999.9628253>.
- Thakkar, M., A. Busse, and N. Sandham. 2017. "Surface correlations of hydrodynamic drag for transitionally rough engineering surfaces." *J. Turbul.* 18 (2): 138–169. <https://doi.org/10.1080/14685248.2016.1258119>.
- Townsend, A. A. 1976. *The structure of turbulent shear flow*. 2nd ed. Cambridge, UK: Cambridge University Press.
- Volino, R. J., M. P. Schultz, and K. A. Flack. 2011. "Turbulence structure in boundary layers over periodic two- and three-dimensional roughness." *J. Fluid Mech.* 676 (Jun): 172–190. <https://doi.org/10.1017/S0022112011000383>.
- von Kármán, T. 1930. "Mechanische Ähnlichkeit und turbulenz." *Nachrichten von der Gesellschaft der Wissenschaften zu Göttingen, Mathematisch-Physikalische Klasse* 1930 (CWTK 2): 322–336.
- Yuan, J., and U. Piomelli. 2014. "Roughness effects on the Reynolds stress budgets in near-wall turbulence." *J. Fluid Mech.* 760 (Dec): R1. <https://doi.org/10.1017/jfm.2014.608>.
- Yuan, J., and U. Piomelli. 2015. "Numerical simulation of a spatially developing accelerating boundary layer over roughness." *J. Fluid Mech.* 780 (Oct): 192–214. <https://doi.org/10.1017/jfm.2015.437>.